Nationaal Lucht- en Ruimtevaartlaboratorium

National Aerospace Laboratory NLR

Executive summary

Using phased array beamforming to locate broadband noise sources inside a turbofan engine

Problem area
Reduction of fan-broadband noise from aircraft engines.

Description of work
A feasibility study was performed on the application of "phased array" techniques to locate sound sources on the rotor and the stator of turbofan aircraft engines, using microphone arrays in the inlet.

Results and conclusions
The feasibility has been demonstrated.

Applicability
Design of low-noise aircraft components.

Using phased array beamforming to locate broadband noise sources inside a turbofan engine

Nationaal Lucht- en Ruimtevaartlaboratorium, National Aerospace Laboratory NLR

Anthony Fokkerweg 2, 1059 CM Amsterdam,
P.O. Box 90502, 1006 BM Amsterdam, The Netherlands
Telephone +31 20 511 31 13, Fax +31 20 511 32 10, Web site: www.nlr.nl

NLR-TP-2006-320

Using phased array beamforming to locate broadband noise sources inside a turbofan engine
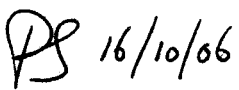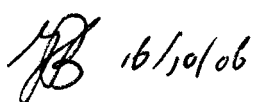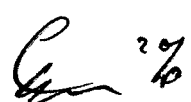
P. Sijtsma

This report is based on a presentation held at the AARC Engine Noise Phased Array Workshop, Cambridge, MA, USA, 11-12 May 2006.

This publication has been refereed by the Advisory Committee AEROSPACE VEHICLES.

Summary

This report discusses the ability of phased arrays to locate forward radiating noise sources on rotors and stators of turbofan engines. Phased array techniques are applied to fan rig measurements with a circular microphone array in the engine intake duct wall, which is normally used for azimuthal mode detection. Beamforming methods are applied with both stationary and rotating focus. The contributions of tonal noise and broadband noise are considered separately. The free-field Green's function is used for the definition of the steering vectors. Special attention is paid to the properties of an unknown source of fan noise.

Contents

Nomenclature

<u>Symbols</u>

A	source power
a	source amplitude
B	number of rotor blades
$\mathbf{C}$	cross-spectral matrix
C_{nm}	cross-power
c	sound speed
$\vec{e}_x$	unit vector in x-direction
F	transfer function
f	frequency
f_{sam}	sample frequency
G	Green's function
g_n	pressure amplitude induced by unit point source
i	imaginary unit
K	number of samples during one revolution
$\vec{M}$	Mach vector
m	mode number
N	number of microphones
p	acoustic pressure
p_n	complex pressure amplitude
t	(receiver) time
t_n	receiver time at n-th microphone
t_v	sample time
$\vec{U}$	flow speed
V	number of stator vanes
$\vec{v}$	see Eq. (17)
$\vec{w}$	see Eq. (18)
$\vec{x}$	receiver location
$\vec{x}_n$	microphone location
β	see below Eq. (5)
$\chi_n(t)$	acoustic pressure at microphone location
χ_v	sampled acoustic pressure
Δt_e	emission time delay
δ	Dirac-delta function
ϕ_j	pulse times

ν sample number

$\nu_{\max}$ see Eq. (23)

$\nu_{\min}$ see Eq. (23)

θ azimuthal angle

σ emitted signal

τ emission time

$\vec{\xi}$ (potential) source location

$\vec{\xi}_0$ reference source location

ψ rotor angle

Ω angular rotor speed

ω angular frequency ($2\pi f$)

Abbreviations

BPF Blade Passing Frequency

EO Engine Order

RPM Revolutions Per Minute

SPL Sound Pressure Level

1 Introduction

Through better design and the use of higher bypass ratios, aircraft turbofan engine noise has been substantially reduced over the last decades. As a consequence, on modern aircraft (e.g. the Airbus A340) many other noise sources, like slats, flaps, and landing gears, have comparable strengths. Nevertheless, even in the landing phase, the engines are still the loudest noise sources (Ref. 1). Therefore, there is a continuous need to further reduce engine noise.

Engine noise can be tonal (buzz-saw noise, rotor alone noise, fan-stator interaction, blade row interaction in the turbine), and broadband (jet noise, fan-broadband noise). Tonal noise and jet noise have been extensively studied, but fan-broadband noise is a rather unexplored area.

At lower engine speeds, typically during approach, fan-broadband noise is a major component of the total noise emitted from turbofan engines. This broadband noise can be caused by various possible mechanisms: interaction of the intake duct boundary layer with the rotor blade tips, interaction of the turbulent rotor wakes with the stator vanes, rotor blade self noise (trailing edge noise), and stator vane self noise.
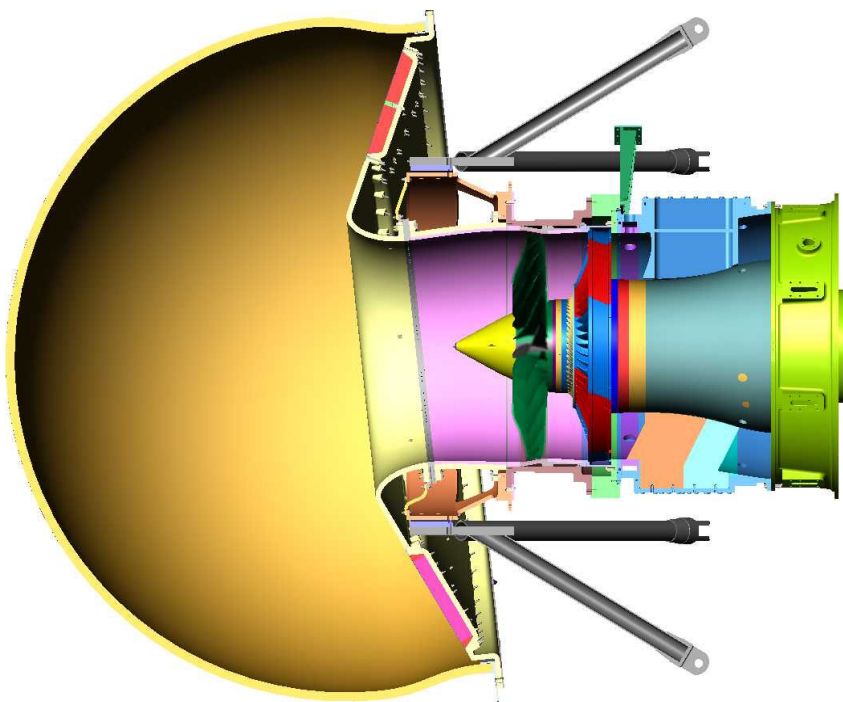

Fig. 1 Drawing of fan rig; the Kulite sensor array is located on the grey strip in the intake

For investigations of broadband noise reduction devices, it is important to know which of the above-mentioned source mechanisms prevail. Unfortunately, there is no straightforward recipe to locate these sources experimentally, and to estimate their strengths. A possible tool may be

the phased array beamforming technique, which has become a standard tool for acoustic source location in wind tunnel and flight testing.

Application of a microphone array inside a turbofan engine is more complicated than at a certain distance. First, there is limited freedom in microphone positioning, as the microphones are not supposed to disturb the flow. Possible microphone positions are the duct wall, the turbulence control screen (TCS), and the stator vanes. A second complication is that the free-field Green's function may not be the most appropriate transfer function for defining the steering vectors, as it neglects the reflections of the duct wall. It may be better to use numerically calculated Green's functions which include the presence of the nacelle. But, nonetheless, inaccuracies will remain, because these Green's functions do no include the (often unknown) source directivities.
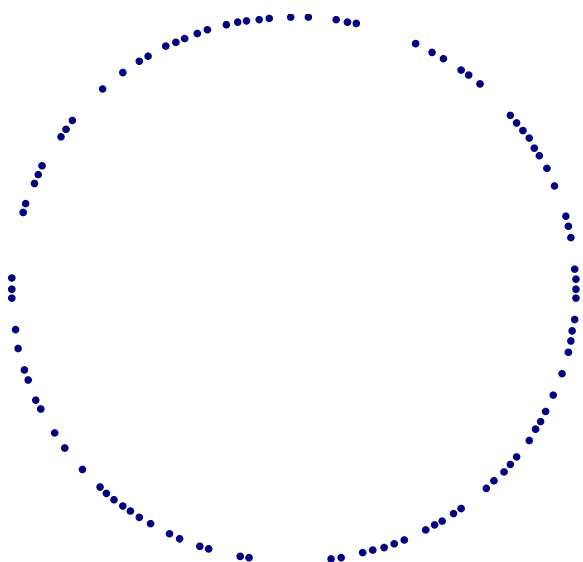
Fig. 2 Lay-out of intake microphone array

In this report, the beamforming techniques as applied to experimental results with a Rolls-Royce fan rig in the AneCom-Aerotest facility near Berlin (Ref. 2) are described. Measurements were done with a circular array of microphones mounted in the intake (Fig. 1), which is drooped. This array, which consists of 100 Kulite sensors, is designed and used for azimuthal mode detection. It has a non-uniform lay-out (Fig. 2), in order to extend the range of modes to be detected (Ref. 3).

The beamforming techniques are tested on a reference case with low engine speed (50 %). A liner was installed between the fan and the array. The auto-spectrum, averaged over all array

microphones, is plotted in figure 3. The peaks at BPF (Blade Passing Frequency) and higher harmonics are clearly visible. Also visible are puzzling humps next to BPF and 2BPF.

In the following chapters, beamforming techniques with stationary and rotating focus are described, and applied to the reference test. Then, a breakdown is given into tonal and broadband noise. Finally, some further investigations are described on the humps as plotted in figure 3.
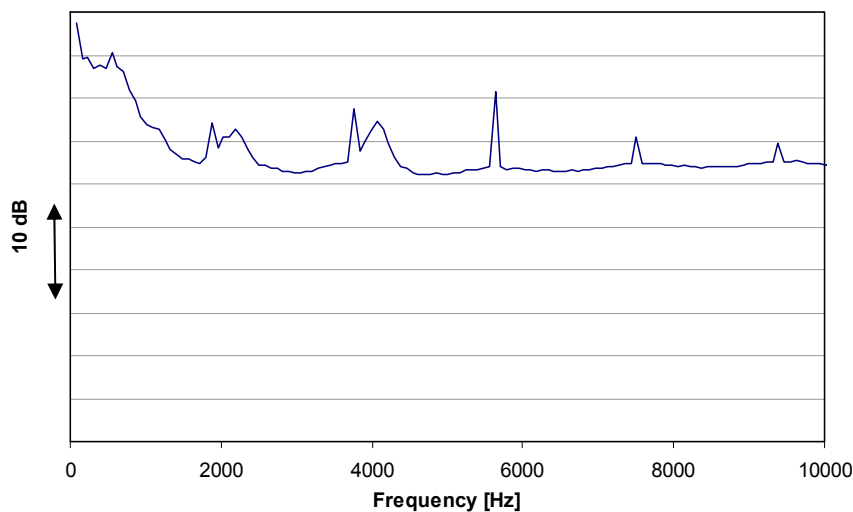

Fig. 3 Average auto-spectrum at microphone array

2   Beamforming

2.1   Stationary focus

2.1.1   Conventional beamforming

With the conventional beamforming technique, noise source maps are constructed as follows. A "scan" is made over a "source" plane, i.e., a plane where acoustic sources are assumed to be located. On each point $\vec{\xi}$ of this scan plane, a point source of unit strength is imagined. An imaginary point source like that induces imaginary acoustic spectra on each microphone.

Now consider a given frequency, and say that g_n is the (complex) pressure amplitude at microphone n, induced by a unit source in $\vec{\xi}$. The conventional beamforming technique compares how well these *imaginary* pressure amplitudes match with the *measured* counterparts p_n. This is done by minimising:

$$J = \sum_{n=1}^{N} \left| p_n - ag_n \right|^2 , \tag{1}$$

where N is the number of microphones and a is the reconstructed source amplitude in $\vec{\xi}$. The solution of this minimisation problem is:

$$a = \sum_{n=1}^{N} g_n^* p_n \left/ \sum_{n=1}^{N} g_n^* g_n \right. . \tag{2}$$

After squaring and averaging, an expression is obtained featuring the cross spectral matrix **C**:

$$A = \frac{1}{2}\left\langle |a|^2 \right\rangle = \sum_{n=1}^{N}\sum_{m=1}^{N} g_n^* \frac{1}{2}\left\langle p_n p_m^* \right\rangle g_m \left/ \left(\sum_{n=1}^{N} g_n^* g_n \right)^2 \right. = \sum_{n=1}^{N}\sum_{m=1}^{N} g_m C_{nm} g_n^* \left/ \left(\sum_{n=1}^{N} g_n^* g_n \right)^2 \right. . \tag{3}$$

At those points $\vec{\xi}$ on the scan plane where the values for A are the highest, actual noise sources may be assumed.

The technique described above assumes that the acoustic sources are concentrated in points. In other words, the spatial extent of the sources is assumed to be zero, which may be a violation of the actual situation. In most beamforming applications, however, this is not a serious limitation.

2.1.2 Point sources

A more critical issue is the propagation from the assumed point source to the microphones, in other words, the construction of the induced pressure amplitudes g_n. In external array applications, usually a free space Green's function G is used, i.e., the solution of the (convective) Helmholtz equation with a Dirac-delta function in the right-hand side:

$$\nabla^2 G - \frac{1}{c^2}\left(2\pi i f + \vec{U} \cdot \frac{\partial}{\partial x} \right)^2 G = -\delta(\vec{x} - \vec{\xi}), \tag{4}$$

where ∇ is the Nabla-operator, c is the speed of sound, $\vec{U}$ is the wind speed, and $\vec{x}$ is the receiver (microphone) location. The solution of (4) is

$$G = \frac{\exp\left[-2\pi i f \Delta t_e \right]}{4\pi \sqrt{\left\{ \vec{M} \cdot \left(\vec{x} - \vec{\xi} \right) \right\}^2 + \beta^2 \left\| \vec{x} - \vec{\xi} \right\|}} , \tag{5}$$

with $\vec{M} = \vec{U}/c$, $\beta^2 = 1 - \left\| \vec{M} \right\|^2$, and

$$\Delta t_e = \frac{1}{c\beta^2}\left(-\vec{M}\cdot\left(\vec{x}-\vec{\xi}\right)+\sqrt{\left\{\vec{M}\cdot\left(\vec{x}-\vec{\xi}\right)\right\}^2+\beta^2\left\|\vec{x}-\vec{\xi}\right\|}\right). \tag{6}$$

Apart from the earlier mentioned point source assumption, the source description of Eq. (5) lacks the following:

    a) It neglects any reflections (engine nacelle, intake plane, spinner).

    b) It assumes uniform flow conditions.

    c) It assumes a source with uniform directivity.

Nevertheless, this "free-field" Green's function will be used for beamforming. In order to reduce the effects of reflections, measurements with a liner (as we use here) are preferred.

A Green's function of a flow duct (expressed in duct modes) would partly remove drawback a) (no reflections), but then a purely cylindrical geometry is assumed, neglecting the effects of droop, spinner and flow non-uniformities. Thus, the remedy could be worse than the disease.

Green's function values may also be calculated by CAA methods. If this is done at sufficiently high accuracy, it would remove drawbacks a) and b), but drawback c) remains. Precise knowledge is then required of the flow field, and, if a liner is present, of the wall impedance. Maybe, it is also possible to determine the Green's function values by measurements, but this does not remove drawback c) either.

2.1.3 Beam patterns

Obviously, a ring-shaped array as in figure 2 is not ideal for source location. Commonly, arrays for beamforming cover a disk-shaped area (e.g. in spiral forming groups) or are cross-shaped. To investigate the beamforming properties of the array, the beam patterns of a simulated point source are considered for a range of 1/3 octave band frequencies. The scan plane is at the leading edge of the stator, and the point source is on the scan plane.

The beam patterns are plotted in figure 4 at a range of 10 dB. The circles in the plots correspond to the tip of the rotor, and to the splitter. (The inner circle is also close to the rotor hub.) The dynamic range (peak level minus highest side lobe level) of the array is about 7 dB. Commonly, arrays for beamforming have higher dynamic range (~ 12 dB). Nevertheless, a dynamic range of 7 dB is still high enough for conducting some beamforming attempts.
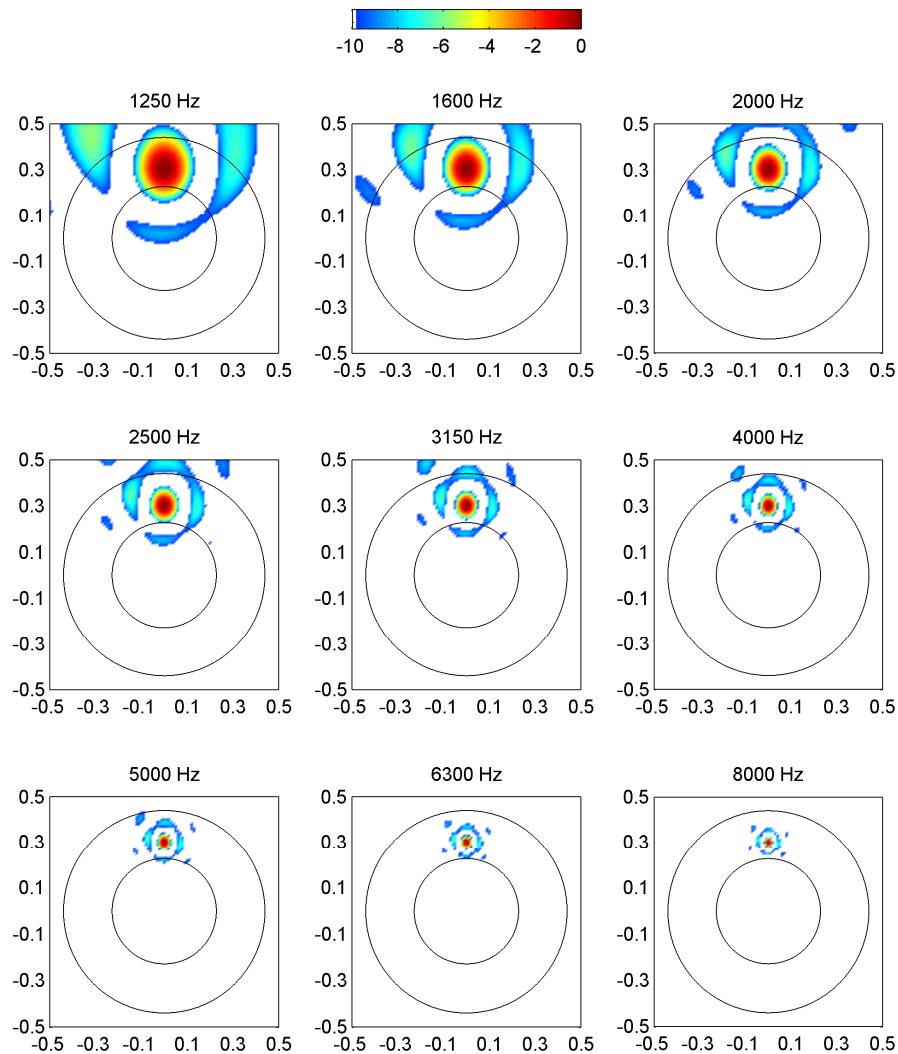
Fig. 4 *Results of conventional beamforming with simulated point source near the rotor trailing edge (beam patterns)*

2.1.4 Results

Results with the conventional beamforming method (neglecting microphone auto-powers) are shown in figure 5 and figure 6. In figure 5, the scan plane is at the leading edge of the *rotor*, and in figure 6 at the leading edge of the *stator*. The lack of axi-symmetry in the plots can be related to the droop of the intake (Fig. 1).

Comparing both figures shows that the radial position of the sources depends on the axial position of the scan plane. This is a consequence of the ring-shape and the position of the array. With this array set-up, it is not possible to determine the axial location of the sources.

At 4000 Hz, 5000 Hz and 6300 Hz, the stator vanes are clearly visible as noise sources. It is likely that figure 6 gives a better indication of the source locations than figure 5. These source locations seem to be near the tips. At lower frequencies, the noise seems to be generated at or close to the splitter.

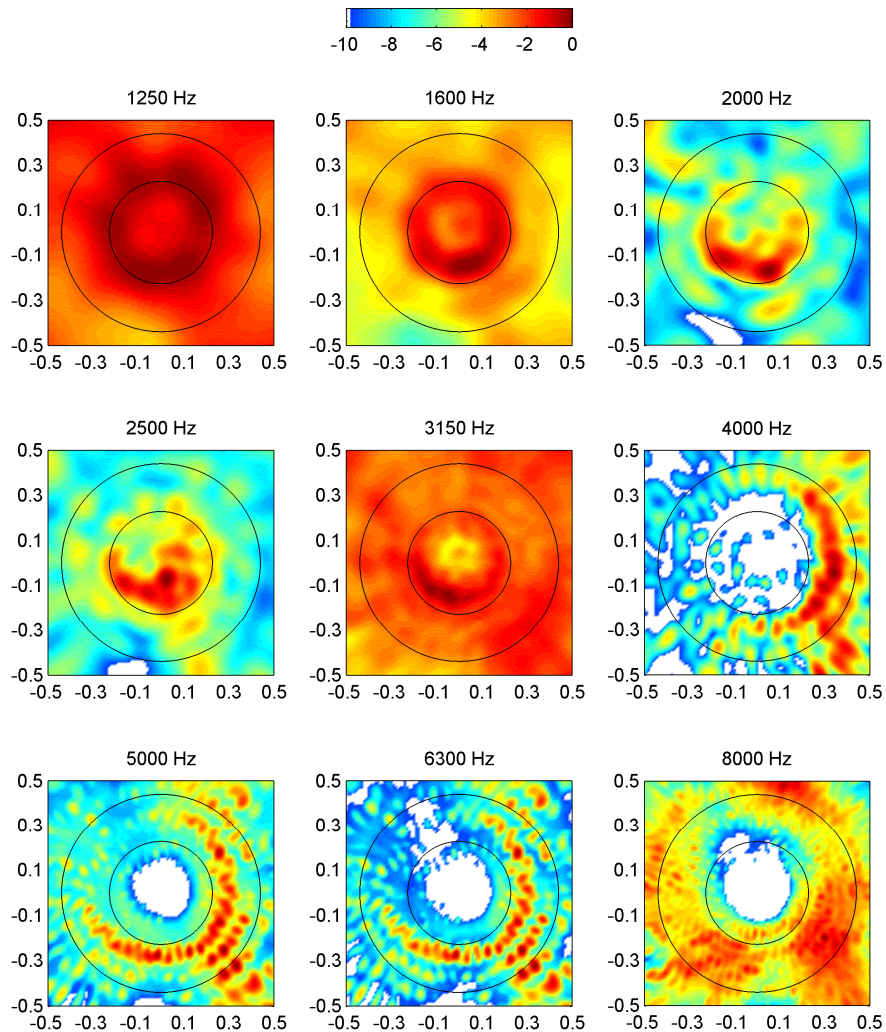The sizes of the source spots in figure 6 are comparable to the simulated results in figure 4.

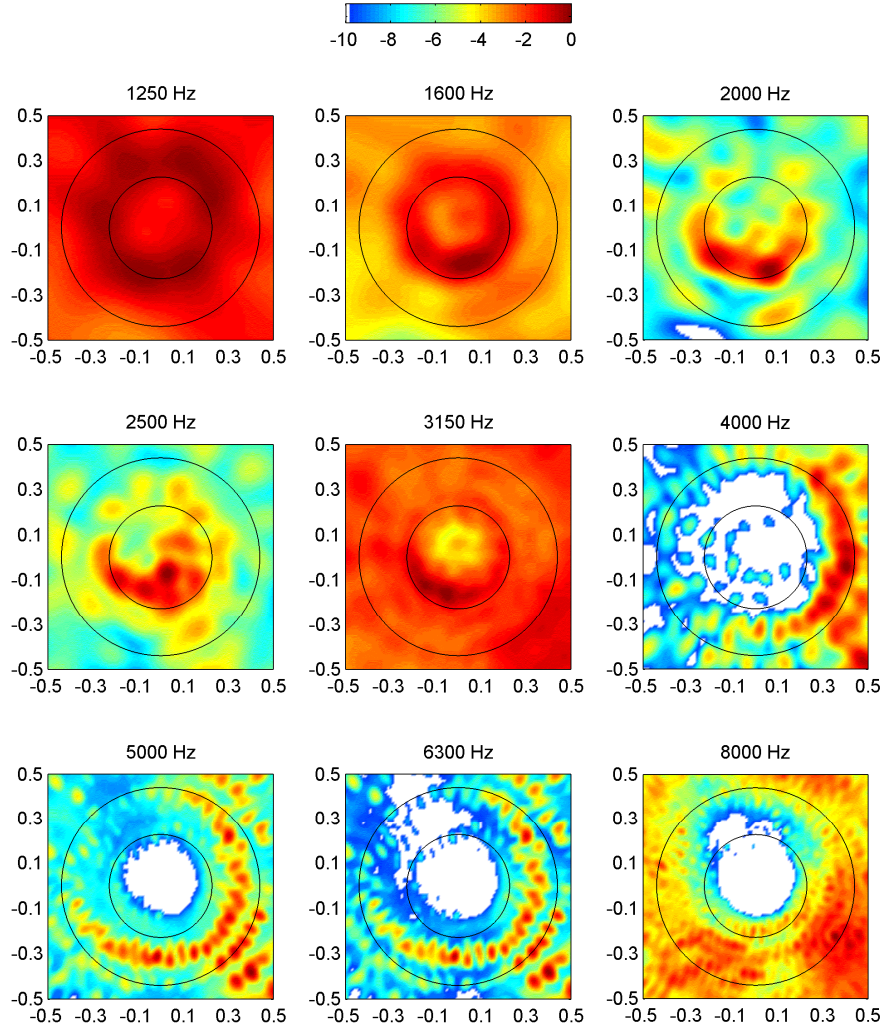*Fig. 5 Results of conventional beamforming on rotor leading edge plane*

Fig. 6 *Results of conventional beamforming on stator leading edge plane*

2.2   Rotating focus

2.2.1   Beamforming on moving sources

With a moving source, at $\vec{\xi}(t)$, it is no longer possible to apply beamforming techniques in the frequency domain. Instead of reconstructing source amplitudes at given frequencies, we have to reconstruct directly the signal $\sigma(t)$ emitted by the source. The source assumption is now described by:

$$\nabla^2 G - \frac{1}{c^2}\left(\frac{\partial}{\partial t} + \vec{U} \cdot \frac{\partial}{\partial x}\right)^2 G = -\sigma(t)\delta\left(\vec{x} - \vec{\xi}(t)\right). \tag{7}$$

14

The solution of Eq. (7), which is derived in Ref. 4, reads:

$$G(\vec{x},t) = \sigma(\tau) \big/ F\left(\vec{x}, \vec{\xi}(\tau), t, \tau\right), \tag{8}$$

with

$$F\left(\vec{x}, \vec{\xi}(\tau), t, \tau\right) = 4\pi \left\{ c(t-\tau) + \frac{1}{c}\left(-\vec{\xi}'(\tau) + \vec{U}\right) \cdot \left(\vec{x} - \vec{\xi}(\tau) - \vec{U}(t-\tau)\right) \right\}, \tag{9}$$

$$t = \tau + \frac{1}{c\beta^2}\left(-\vec{M} \cdot \left(\vec{x} - \vec{\xi}(\tau)\right) + \sqrt{\left\{\vec{M} \cdot \left(\vec{x} - \vec{\xi}(\tau)\right)\right\}^2 + \beta^2 \left\|\vec{x} - \vec{\xi}(\tau)\right\|^2}\right). \tag{10}$$

If $\chi_n(t)$ is the pressure fluctuation measured by the n-th microphone, then $\sigma(\tau)$ can be reconstructed by the "Delay and Sum" method:

$$\sigma(\tau) = \frac{1}{N} \sum_{n=1}^{N} \sigma_n(\tau), \tag{11}$$

$$\sigma_n(\tau) = \chi_n(t_n) F\left(\vec{x}_n, \vec{\xi}(\tau), t_n, \tau\right), \tag{12}$$

$$t_n = \tau + \frac{1}{c\beta^2}\left(-\vec{M} \cdot \left(\vec{x}_n - \vec{\xi}(\tau)\right) + \sqrt{\left\{\vec{M} \cdot \left(\vec{x}_n - \vec{\xi}(\tau)\right)\right\}^2 + \beta^2 \left\|\vec{x}_n - \vec{\xi}(\tau)\right\|^2}\right). \tag{13}$$

Source powers in the frequency domain can be obtained through Fourier transformation of $\sigma(\tau)$, and averaging:

$$A = \frac{1}{2}\left\langle \left|\hat{\sigma}\right|^2 \right\rangle = \frac{1}{2N^2}\left\langle \sum_{n=1}^{N}\sum_{m=1}^{N} \hat{\sigma}_n \hat{\sigma}_m^* \right\rangle, \tag{14}$$

where $\hat{\sigma}$ is the Fourier transform of σ. Results without auto-powers can be obtained by evaluating (14) as:

$$A = \frac{1}{2N(N-1)}\left\langle \sum_{n=1}^{N}\sum_{\substack{m=1 \\ m \neq n}}^{N} \hat{\sigma}_n \hat{\sigma}_m^* \right\rangle. \tag{15}$$

2.2.2 Source tracking

It is assumed that the axis of rotation coincides with the *x*-axis. Then, in the case of a rotating fan, the position of moving sources can be described by:

$$\vec{\xi}(\tau) = \left(\vec{\xi}_0 \cdot \vec{e}_x\right)\vec{e}_x + \cos\left(\psi(\tau)\right)\vec{v} + \sin\left(\psi(\tau)\right)\vec{w}, \tag{16}$$

with

$$\vec{v} = \vec{\xi}_0 - \left(\vec{\xi}_0 \cdot \vec{e}_x\right)\vec{e}_x, \tag{17}$$

$$\vec{w} = \vec{e}_x \times \vec{v}, \tag{18}$$

and $\vec{e}_x$ is the unit vector in *x*-direction. The source position at $\psi(\tau) = 0$ is given by $\vec{\xi}_0$.
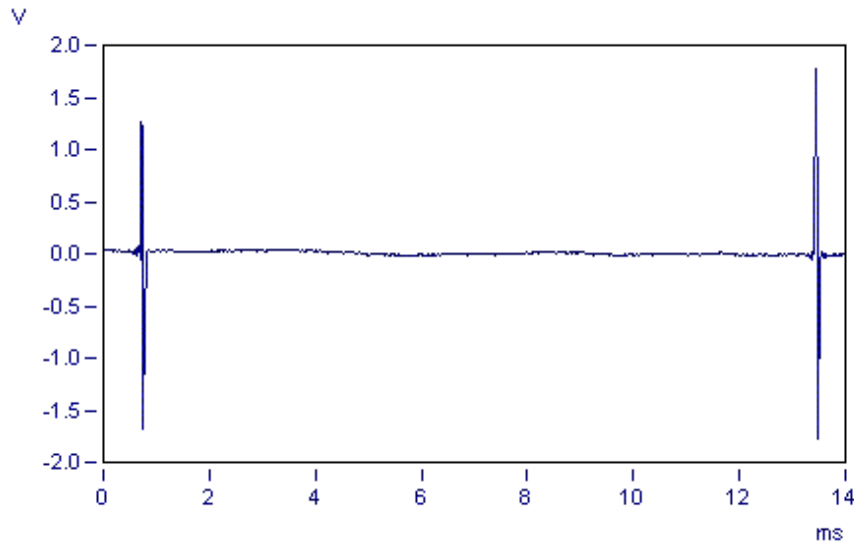

Fig. 7 Pulse signal

The time-dependent angles $\psi(\tau)$ are derived using a tacho pulse generator which gives a pulse for every rotor revolution. This pulse signal (see Fig. 7) is stored in one of the channels of the data-acquisition system. Using a technique based on cross-correlations, pulse times ϕ_j are calculated. Herewith, the time-dependent RPM can be calculated at a relative accuracy of less than 0.01% (see Fig. 8). Using these pulse times, we can define:

$$\psi(\tau) = 2\pi \frac{\tau - \phi_{j-1}}{\phi_j - \phi_{j-1}}. \tag{19}$$

Thus, by definition, $\psi(\tau) = 0$ at the pulse times ϕ_j. The beamforming process starts with the choice of a basic scan grid of possible source locations $\vec{\xi}_0$, which are the locations of the rotating sources at the pulse times. The rotation is then described by Eqs. (16)-(19).
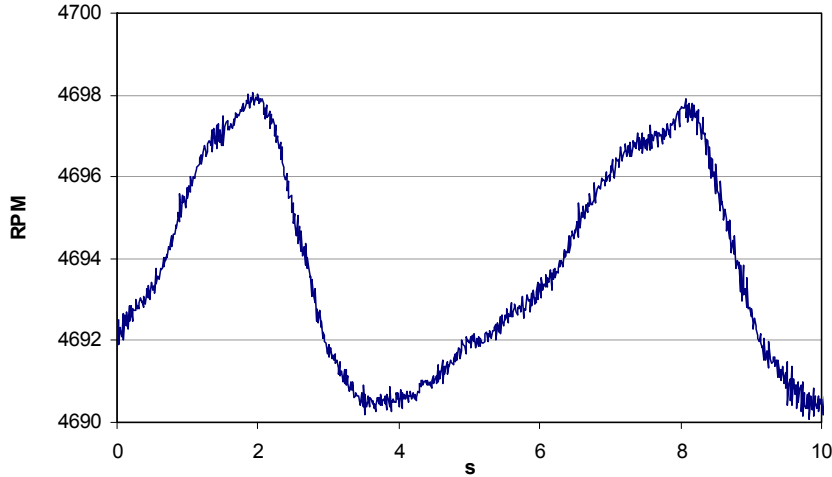

Fig. 8 Development of RPM as calculated from pulse signal

Each emission time period $\left[\phi_{j-1}, \phi_j \right]$ is sampled into K samples:

$$\tau_k = \phi_{j-1} + \frac{k}{K}(\phi_j - \phi_{j-1}), \ k = 0,...,K-1, \tag{20}$$

where K is chosen such that the sampling rate $K/(\phi_j - \phi_{j-1})$ is approximately the same as the sampling frequency f_{sam} of the measured data. The corresponding rotation angles are:

$$\psi_k = \psi(\tau_k) = 2\pi k/K . \tag{21}$$

Using Eqs. (11)-(13), with $\tau = \tau_k$, the sample values of the emitted signal σ can be obtained. Then, with (14) or (15) the source spectra can be calculated.

2.2.3 Results

Results of the beamforming technique with rotating focus (without auto-powers) are shown in figure 9. At the frequency bands 2500 Hz, 3150 Hz, and 4000 Hz, the rotor blades are visible. In figure 10, the (narrow-band) peak values of the source plots are compared with corresponding results of the conventional beamforming method (at the same scan plane, see Fig. 5). With rotating focus, the BPF-peaks have disappeared. On the other hand, the non-BPF levels seem to be somewhat higher. On the second hump location (approximately 4 kHz), a peak is found which is narrower than the hump.
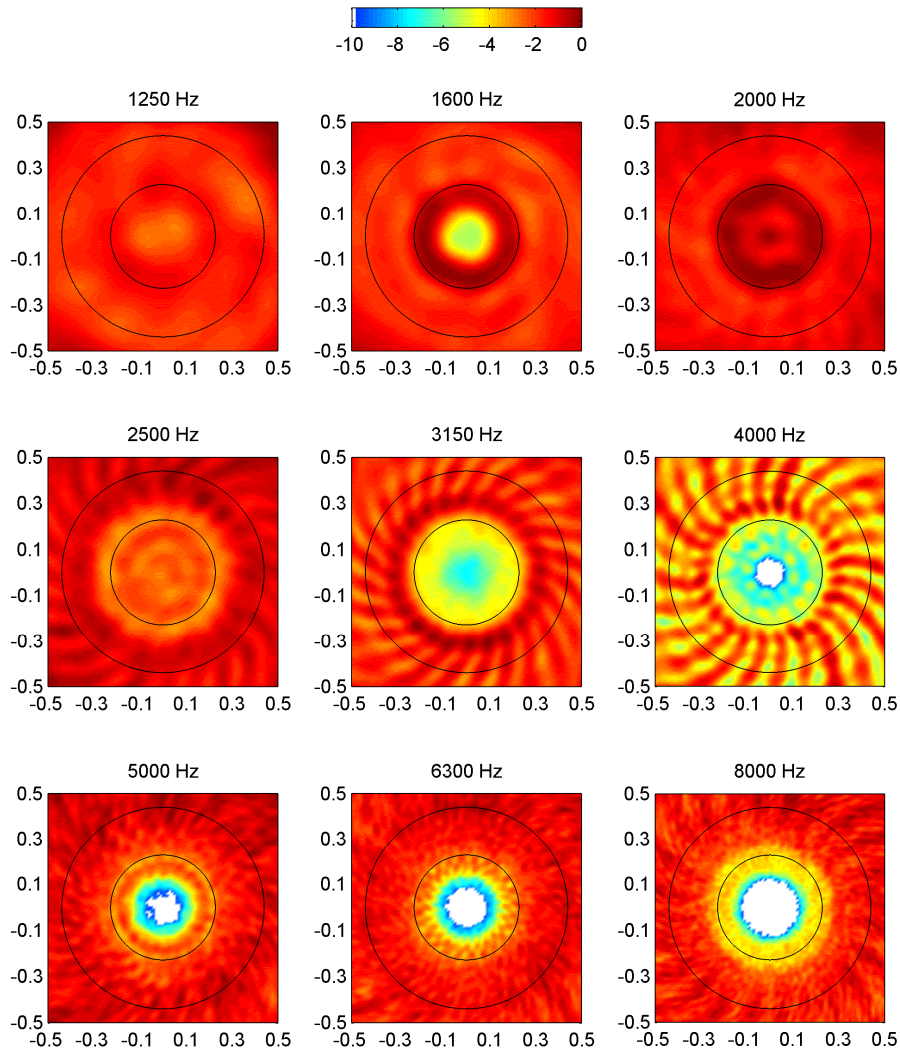
17

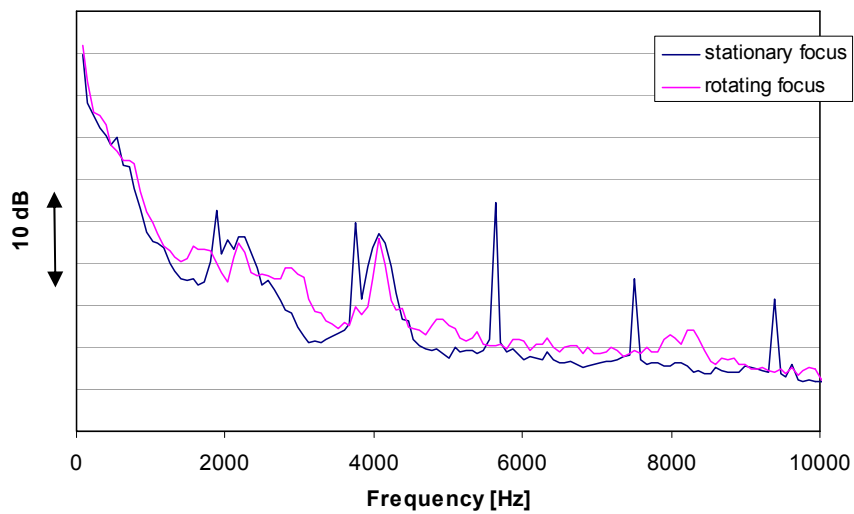Fig. 9 *Results of beamforming with rotating focus on rotor leading edge plane*

Fig. 10 *Narrow-band peak values of beamforming results – stationary vs rotating focus*

18

3 Tonal and broadband noise

3.1 Splitting technique

Part of the noise signal, as measured by the microphones, is repeated every rotor revolution. If the RPM is constant, then this "rotor-bound" noise consists of pure tones, of which the frequencies are multiples of the revolution frequency. At low engine speeds, when the fan tip speed is subsonic, usually only the BPF (revolution frequency × number of rotor blades) and its higher harmonics appear in the spectrum.

The rotor-bound noise is extracted from the total noise with the following method. Let

$$\chi_v = \chi(t_v) = \chi(v/f_{\text{sam}}) \tag{22}$$

be the sampled values of the measured noise signal by one of the microphones. Consider a series of samples between two pulse times:

$$\phi_{j-1} \leq t_{v_{\min}} < t_{v_{\min}+1} < ... < t_{v_{\max}} < \phi_j . \tag{23}$$

Fourier components are calculated by:

$$p_k = \frac{2}{v_{\max}-v_{\min}+1} \sum_{v=v_{\min}}^{v_{\max}} \chi_v \exp\left[-2\pi ik\left(t_v - \phi_{j-1}\right)\big/\left(\phi_j - \phi_{j-1}\right)\right]. \tag{24}$$

These complex numbers are averaged over all revolutions, and then calculated back to the time domain:

$$\chi(t_v) = \sum_{k=1}^{(v_{\max}-v_{\min}+1)/2} p_k \exp\left[2\pi ik\left(t_v - \phi_{j-1}\right)\big/\left(\phi_j - \phi_{j-1}\right)\right]. \tag{25}$$

After the rotor-bound noise has been determined, the broadband noise can be obtained by subtracting the rotor-bound noise from the total noise.

In figure 11 the breakdown into tonal (rotor-bound) and broadband noise is shown of the average microphone auto-spectrum (cf. Fig. 3). Apparently, the humps have a broadband character.
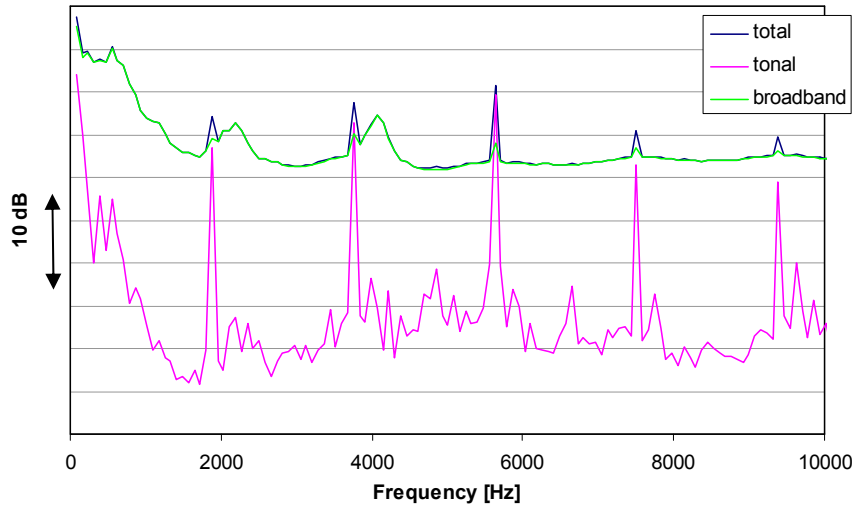
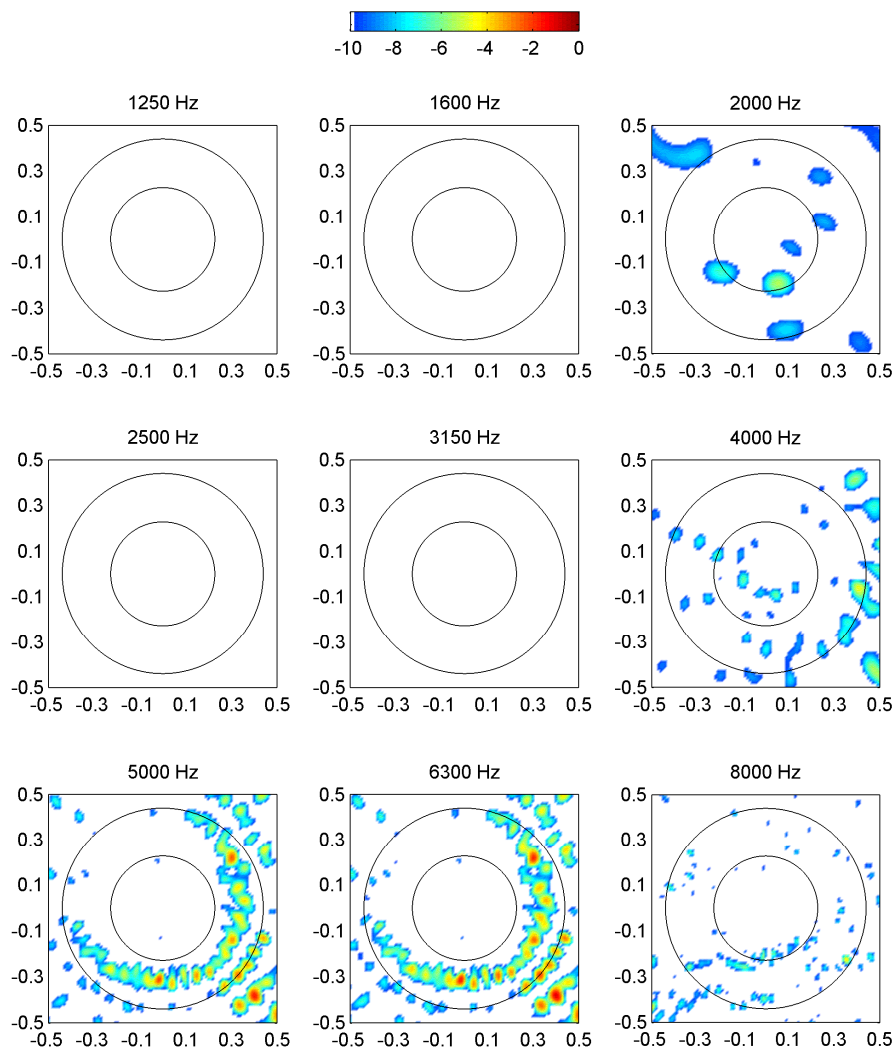*Fig. 11 Average auto-spectrum at microphone array – breakdown into tonal and broadband noise*

Fig. 12 Results of conventional beamforming on stator leading edge plane – tonal noise

3.2 Results with stationary focus

Beamforming results on the stator leading edge plane, after splitting into tonal and broadband noise, are shown in figure 12 and figure 13, respectively. The levels are relative to the levels in figure 6. Tonal noise is dominating at 5000 Hz and 6300 Hz, while broadband noise is prevailing at other frequency bands. Only at 4000 Hz, broadband noise sources on the stator vanes can be observed. This happens to be at the second hump (cf. Fig. 11). The peak values of the narrow-band conventional beamforming results are shown in figure 14. Now the BPF tones protrude more than in figure 11. This could mean that tonal noise is more localized than broadband noise. Also, the humps are more pronounced.
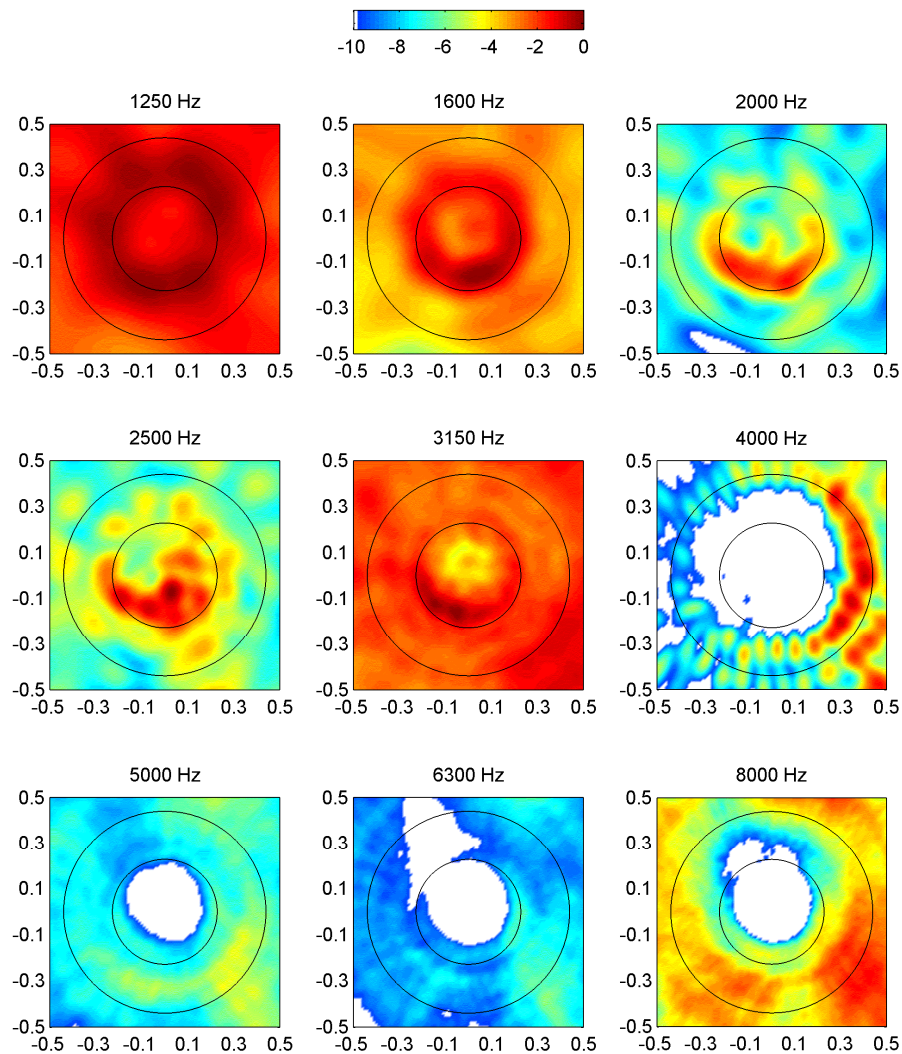
Fig. 13 Results of conventional beamforming on stator leading edge plane – broadband noise
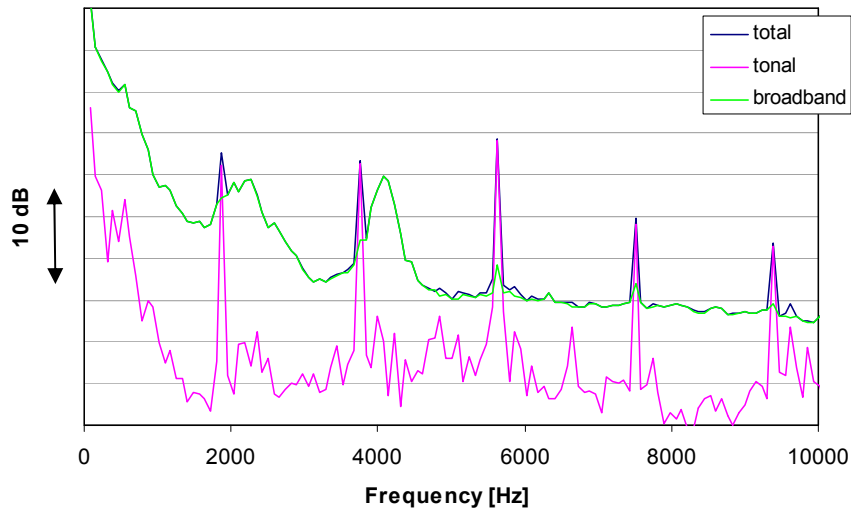
*Fig. 14 Narrow-band peak values of conventional beamforming results –
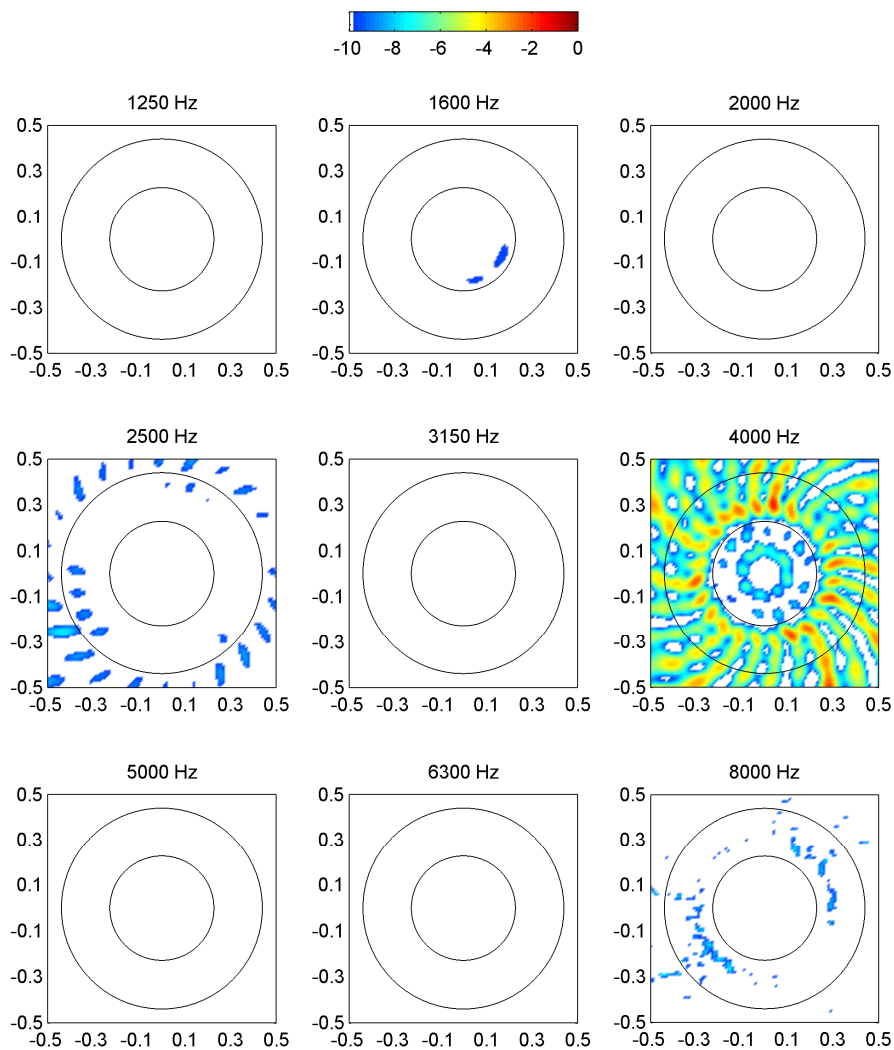breakdown into tonal and broadband noise*

Fig. 15 Results of beamforming with rotating focus on rotor leading edge plane – tonal noise

3.3 Results with rotating focus

Results of beamforming on the rotor leading edge plane with the method of Section 2.2, again after splitting into tonal and broadband noise, are shown in figure 15 and figure 16, where the levels are relative to figure 9. Broadband noise is now dominating, except at 4000 Hz. As in figure 9, the rotor blades are visible as noise sources at the frequency bands 2500 Hz, 3150 Hz, and 4000 Hz, but now we can also vaguely see rotor blade noise sources in higher frequency bands.

The peak values of the beamforming results are shown in figure 17. Remarkably, the tonal noise dominates at frequencies around 4000 Hz, which seems to be in contrast with figure 14. This paradox can be explained with some basic knowledge about rotor-stator interaction noise (Ref. 5), as will be worked out below.

An acoustic mode in a flow duct can be described by:

$$p = p(x,r)e^{i(\omega t - m\theta)}, \tag{26}$$

with $\omega = 2\pi f$. If a mode with $m = m_{\text{in}}$ and $\omega = \omega_{\text{in}}$ interacts with a rotor having B blades and angular frequency Ω, then new acoustic modes are generated with:

$$\begin{cases} \omega_{\text{out}} = \omega_{\text{in}} + \nu B\Omega, \\ m_{\text{out}} = m_{\text{in}} + \nu B, \end{cases} \tag{27}$$

in which ν is any integer. The rotor blades experience unsteady loading, with

$$\omega_{\text{blade}} = \omega_{\text{in}} - m_{\text{in}}\Omega = \omega_{\text{out}} - m_{\text{out}}\Omega . \tag{28}$$

Now consider the mode spectra (tonal noise) at 2BPF ($\omega = 2B\Omega$) and at 3BPF ($\omega = 2B\Omega$). These spectra are plotted in figure 18. At 2BPF, one of the dominant modes is $m = -4$, and at 3BPF the dominant modes are around $m = 20$. These are the well-known rotor-stator interaction modes:

$$m = nB - kV , \tag{29}$$

where n is the BPF order, V is the number of stator vanes, and k is an integer. In our case, we have $B = 24$, $V = 52$, and $k = 1$. When these modes interact with the rotor, we have according to (28):

$$\omega_{\text{blade}} = \omega_{\text{in}} - m_{\text{in}}\Omega = nB\Omega - (nB - V)\Omega = V\Omega .$$

(30)

In other words, the frequency on the rotor is equal to the "vane passing frequency". This is the peak frequency that is observed in figure 17, and there is no direct relation with the second hump in figure 14. The origin of the humps in figure 14 will be further explored in the next chapter.
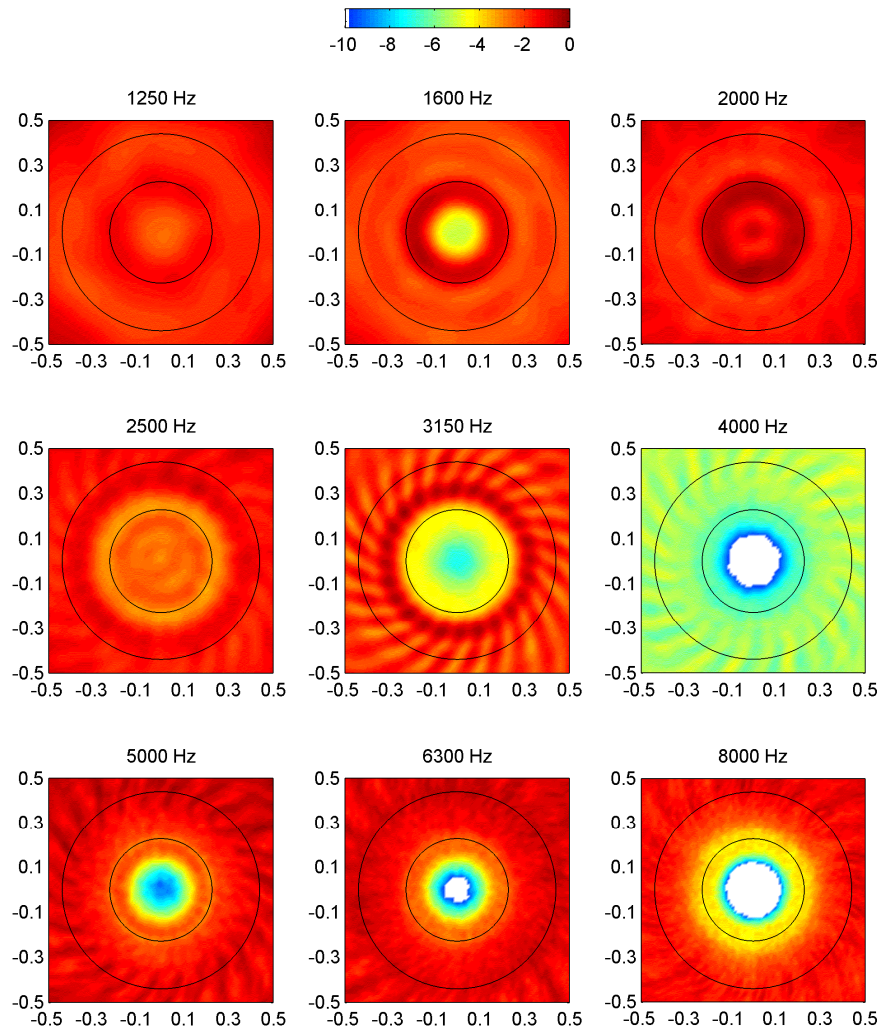

Fig. 16 *Results of beamforming with rotating focus on rotor leading edge plane – broadband noise*
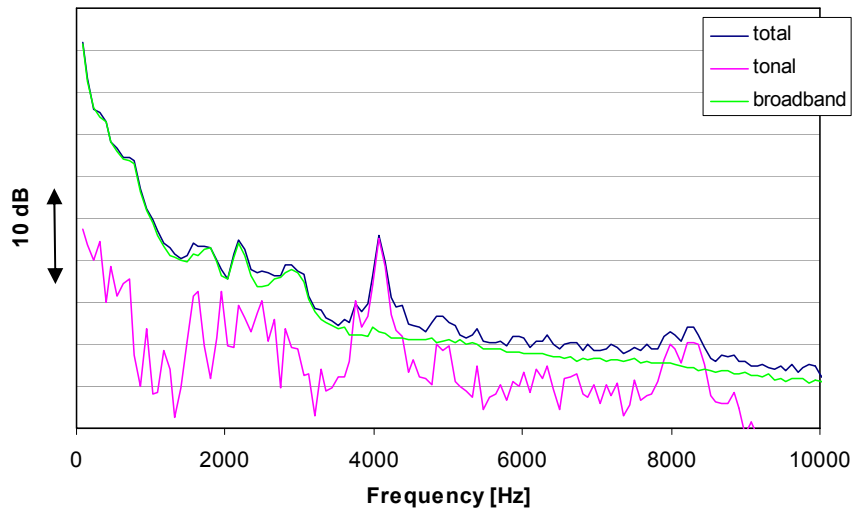
Fig. 17 Narrow-band peak values of beamforming results with rotating focus – breakdown into tonal and broadband noise
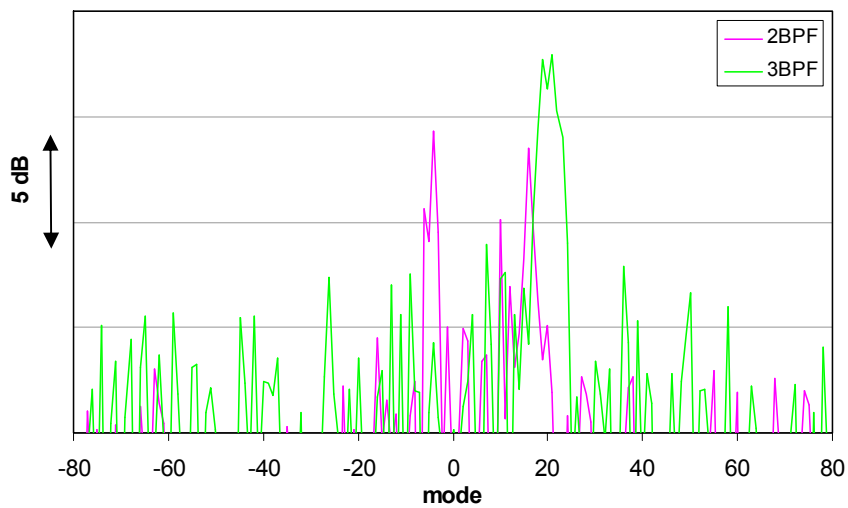

Fig. 18 Mode spectra at 2BPF and 3BPF – tonal noise

4 A closer look to the spectral humps

The origins of the broadband humps in figure 11 are not yet understood, but at least the following can be said about them:

1. Peak frequencies

The peak values of the broadband humps appear at engine orders EO = 26 ($\omega = 26\Omega$, f = 2034 Hz) and EO = 52 ($\omega = 52\Omega$, f = 4068 Hz).

2. Modal content

The mode spectra at the peak frequencies are shown in figure 19. The noise appears to be concentrated in single modes, viz. $m = 4$ at EO = 26 and $m = 15$ at EO = 52.
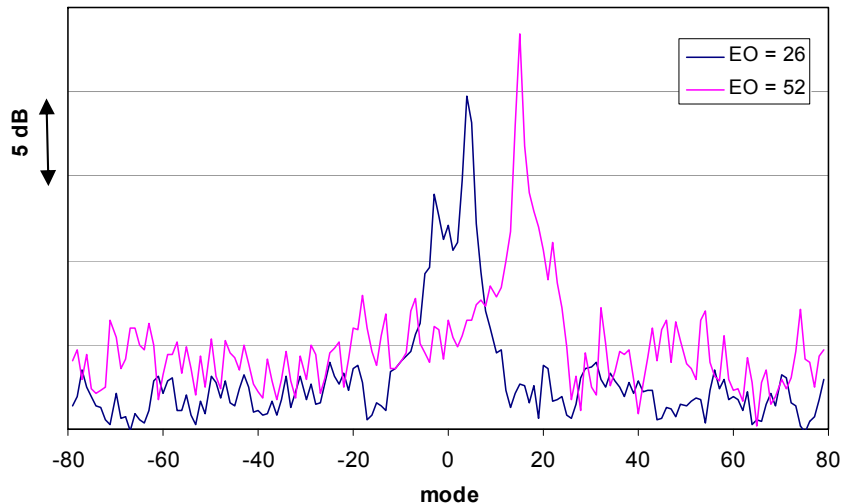

Fig. 19 Mode spectra at 2034 Hz (EO = 26) and at 4068 Hz (EO = 52) – total noise

3. Frequencies at the rotor

According to Eq. (28), the dominating acoustic modes, mentioned above, should correspond with rotor blade loading frequencies at EO = 22 (1721 Hz) and EO = 37 (2895 Hz). Indeed, around those frequencies small humps are visible in figure 17. Between these two humps, there is a third hump around EO = 28 (2190 Hz). This one corresponds with another peak in the mode spectrum of EO = 26 (Fig. 19), namely $m = -3$.
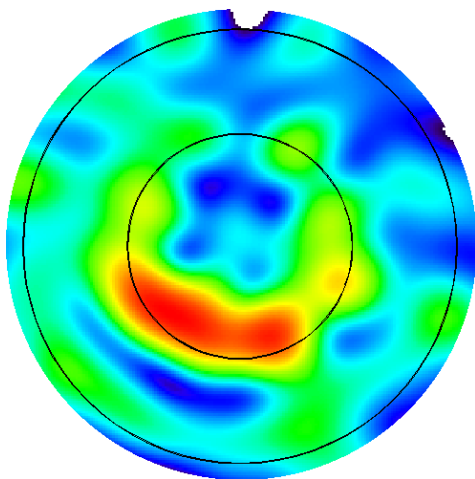

*Fig. 20 Conventional beamforming on stator leading edge
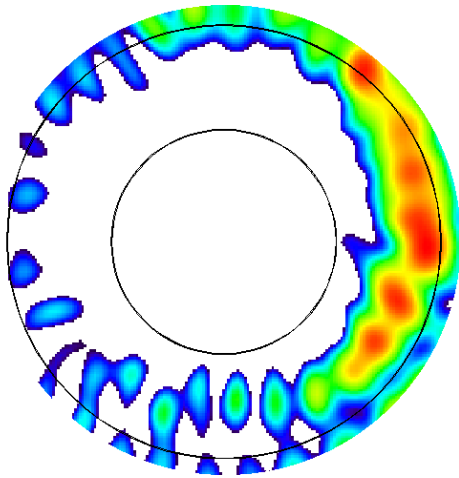plane – broadband noise: narrow-band result at EO = 26*

Fig. 21 Conventional beamforming on stator leading edge
plane – broadband noise: narrow-band result at EO = 52

4. Possible source locations on the stator

Narrow-band conventional beamforming results (scan plane at the stator leading edge) at EO = 26 and EO = 52 are shown in figure 20 and figure 21, respectively. At EO = 26, the sources seem to be located near the splitter. At EO = 52, the sources seem to be located near the tips of the stator vanes. However, looking more closely to figure 21, it seems to be that the number of sources in circumferential direction is less than the number of stator vanes ($V = 52$).
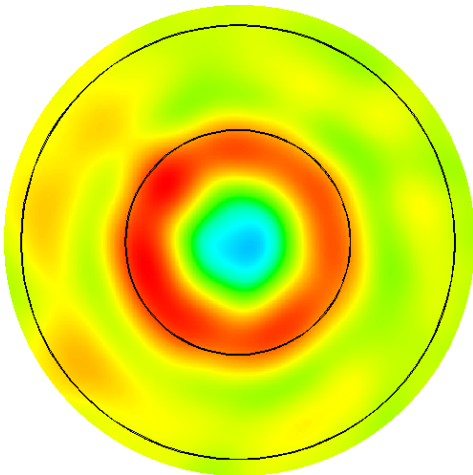

Fig. 22 Beamforming with rotating focus on rotor leading edge
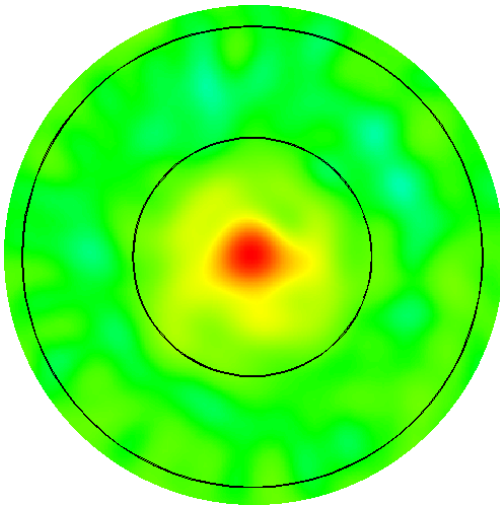*plane – broadband noise: narrow-band result at EO = 22*

*Fig. 23 Beamforming with rotating focus on rotor leading edge
plane – broadband noise: narrow-band result at EO = 28*
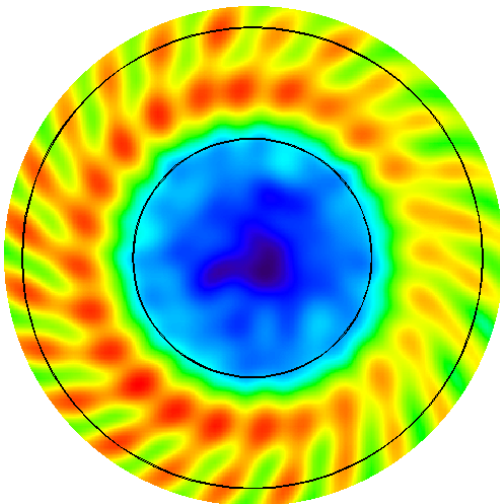
*Fig. 24 Beamforming with rotating focus on rotor leading edge
plane – broadband noise: narrow-band result at EO = 37*

5. Possible source locations on the rotor

Narrow-band beamforming results with rotating focus (scan plane at the rotor leading edge) at
EO = 22, EO = 28, and EO = 37 are shown in figure 22 to figure 24. Each of these plots seem to
show a different noise source mechanism: Figure 22 shows sources around the rotor hub, figure
23 seems to show a source in the middle of the spinner, and figure 24 shows sources on the
rotor blades.

6. Coherence

A surprising feature of the hump at EO = 52 is the single mode behaviour (see Fig. 19). It is shown in figure 21 and in figure 24 that the noise is radiating from many locations. Since the noise is broadband, or at least not rotor-bound, it is natural to expect that all these sources are incoherent. However, with incoherent sources a single non-zero mode would not be expected. Apart from $m = 15$, there should be, at least, also peaks at $m = 0$ and $m = -15$ (Ref. 6).

An estimate of the number of incoherent sources can be made with an eigenvalue analysis of the cross-spectral density matrix of the microphone array. The number of (highest) eigenvalues is a good indication of the number of (loudest) incoherent source components. In figure 25, the 10 highest eigenvalues are plotted, over the entire frequency range. The figure shows that the highest eigenvalue at EO = 52 (and to a smaller extent at EO = 26) is significantly higher than the next eigenvalue, which indicates that the noise is dominating by a single coherent component.
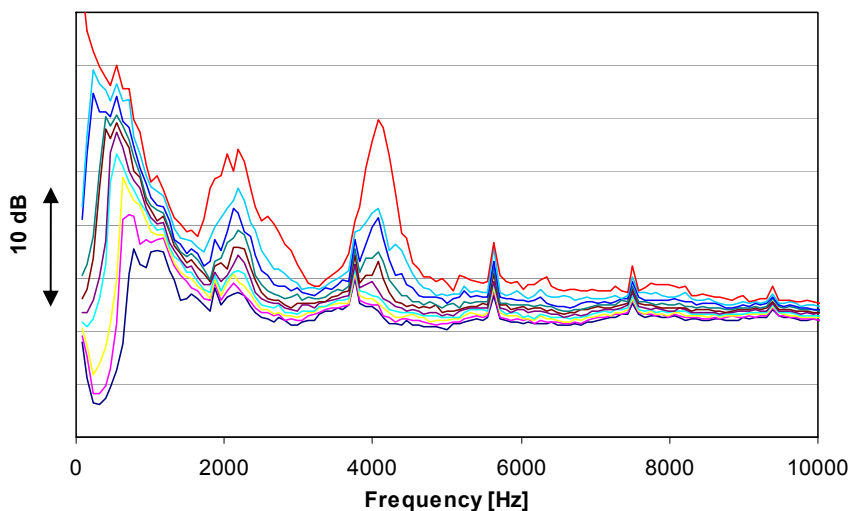
Fig. 25 *Values of 10 highest eigenvalues of microphone array cross-spectral density matrix – broadband noise*

Another way to consider this coherence issue is to look at source coherence in the scan plane (Ref. 7). By considering source coherence, it is possible to remove in a noise source plot all sources that are coherent with the peak source. This is, in fact, one iteration of the alternative CLEAN method (with unit loop gain), as described in Appendix A. This technique is applied to the conventional beamforming results of EO = 26 and EO = 52. The resulting source plots in figure 26 and figure 27 show what is left from figure 20 and figure 21, respectively, after subtracting the main coherent component. Since figure 27 (EO = 52) is virtually empty, all sources shown in figure 20 are apparently coherent.

29
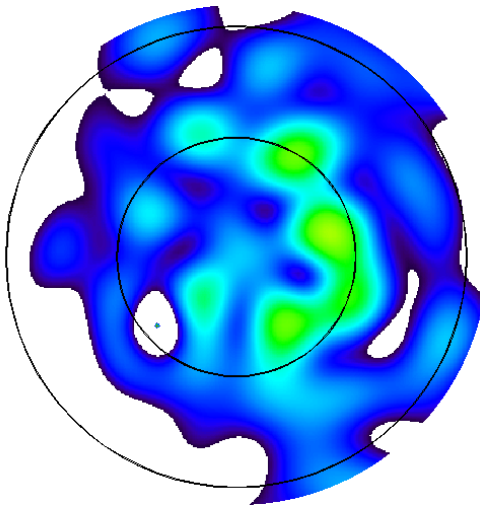
*Fig. 26 Conventional beamforming on stator leading edge*
plane – broadband noise: narrow-band result at
EO = 26 – after subtraction of main coherent component
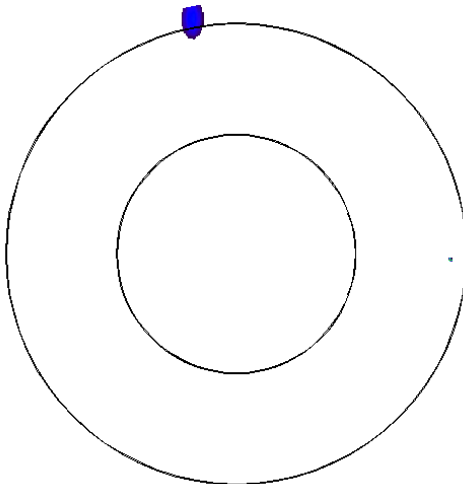
Fig. 27 Conventional beamforming on stator leading edge
plane – broadband noise: narrow-band result at
EO = 52 – after subtraction of main coherent component

7. Possible source mechanism

Using mode detection and phased array techniques, we are able to determine many properties of the source mechanisms causing the spectral humps, like:

- – their broadband (non rotor-bound) nature,
- – their modal content,
- – frequencies of unsteady loading at the rotor,
- – possible source locations on the stator,
- – possible source locations on the rotor,

− their coherent behaviour.

Nonetheless, to the knowledge of the author, the cause for the spectral humps has not been found yet, but with the features mentioned above it should be easier to trace the source origin. The coherent behaviour of the noise sources suggests that it is possibly something like rotor instability.

5 Conclusions

The main conclusions of this report are:
- Application of phased array beamforming techniques, both with stationary and rotating focus, to measurements with a circular intake microphone array is feasible. Noise source locations on both rotor and stator are clearly visible.
- The breakdown into tonal and broadband noise gives valuable additional information.
- Knowledge about the (azimuthal) modal content is very important to understand the beamforming results.

6 Future research

The following future investigations on this subject are envisaged:
- study of the effects of wall reflections,
- study of the effects of an intake liner,
- research into possible improvements by choosing a different array location.

7 Acknowledgements

References

1. Sijtsma, P.: Stoker, R.W.; *Determination of absolute contributions of aircraft noise components using fly-over array measurements*, AIAA Paper 2004-2958, 2004.

2. Müller D.; Schulz H-J.; Zitouni G.; Baumann W.; *Europe's Largest Aero Acoustic Test Facility for Aero-Engine Fans – the Development and Operation of the AneCom AeroTest Anechoic Chamber*, AIAA-2005-3050, 2005.

3. Rademaker, E.R.; Sijtsma, P.; Tester, B.J.; *Mode detection with an optimised array in a model turbofan engine intake at varying shaft speeds*, AIAA Paper 2001-2181, 2001.

4. Sijtsma, P.; Oerlemans S.; Holthusen, H.H.; *Location of rotating sources by phased array measurements*, AIAA Paper 2001-2167, 2001.

5. Tyler, J.M.; Sofrin, T.G.; *Axial flow compressor noise studies*, SAE Transactions, Vol. 70, pp. 309-332, 1962.

6. Tester, B.J.; Sijtsma, P.; Joseph, P.; Lowis, C.; *Fan broadband noise simulation*, AIAA Paper 2006-2684, 2006.

7. Oerlemans, S.; Sijtsma, P.; *Determination of absolute levels from phased array measurements using spatial coherence*, AIAA Paper 2002-2464, 2002.

8. Högbom, J.A.; *Aperture synthesis with a non-regular distribution of interferometer baselines*, Astron. Astrophys. Suppl., No. 15, pp. 417-426, 1974.

Appendix A Source deconvolution using CLEAN

A method of removing a dominant source is CLEAN (Ref. 8), a technique that astronomers use to remove side lobes of bright stars from maps obtained with multiple telescopes. Basically, CLEAN performs the following steps

- It searches for the location of the maximum source auto-power in the acoustic image.
- It subtracts the appropriately scaled theoretical beam pattern of that source ("dirty beam", including side lobes) from the acoustic image.

It replaces this "dirty beam" by a "clean beam" (beam without side lobes).

This process can be done iteratively, for multiple sources. Ignoring the "clean beam" issue, the analysis is as follows.

Suppose that beamforming is expressed in vector notation as:

$$A = \mathbf{w}^*\mathbf{C}\mathbf{w} , \tag{31}$$

where the asterisk means "complex conjugate transpose", $\mathbf{C}$ is a cross-power matrix, and $\mathbf{w}$ a weight vector. This weight vector is derived from a transfer vector $\mathbf{g}$ (e.g. in Eq. (3) we have $\mathbf{w} = \mathbf{g}/\mathbf{g}^*\mathbf{g}$), which points to a source location $\vec{\xi}$. Suppose that $\mathbf{w}_{\max}$ is the weight vector with the maximum 'array output' $A_{\max}$:

$$A_{\max} = \mathbf{w}_{\max}^*\mathbf{C}\mathbf{w}_{\max} . \tag{32}$$

The weight vector $\mathbf{w}_{\max}$ is associated with a transfer vector $\mathbf{g}_{\max}$ and a source location $\vec{\xi}_{\max}$.

A modified array output A_{mod} , without the disturbing influence of the source in $\vec{\xi}_{\max}$ can formally be written as

$$A_{\mathrm{mod}} = \mathbf{w}^*\mathbf{C}\mathbf{w} - \mathbf{w}^*\mathbf{C}_{\max}\mathbf{w} , \tag{33}$$

where $\mathbf{C}_{\max}$ is the cross-power matrix induced by the source in $\vec{\xi}_{\max}$. This matrix $\mathbf{C}_{\max}$ is unknown, but a reasonable guess seems to be:

$$\mathbf{C}_{\max} = A_{\max}\mathbf{g}_{\max}\mathbf{g}_{\max}^* . \tag{34}$$

Equations (33) and (34) form the basis for the CLEAN algorithm, which is as follows:

- Step 1: Apply the beamforming algorithm to the scan plane, search for the peak source location $\vec{\xi}_{\max}$, and determine the corresponding matrix $\mathbf{C}_{\max}$.

- Step 2: Replace the cross-power matrix $\mathbf{C}$ by $\mathbf{C} - \varphi\mathbf{C}_{\mathrm{max}}$, where φ is a safety factor with $0 < \varphi \leq 1$, called the "loop gain".
- Step 3: Return to step 1, unless a certain stop criterion is fulfilled.

Afterwards, the information that has been subtracted in Step 2 can be used to produce a "clean map".

The CLEAN algorithm, as sketched above, is based on the assumption of point sources. Furthermore, it assumes that the sound transfer is well described by $\mathbf{g}_{\mathrm{max}}$. The latter assumption includes a uniform directivity and no loss of coherence, which is seldom fulfilled in aero-acoustic measurements. To overcome this limitation, an alternative approximation for $\mathbf{C}_{\mathrm{max}}$ is proposed below.

The matrix $\mathbf{C}_{\mathrm{max}}$ will be defined such that the source cross-power $A_{1,2} = \mathbf{w}_1^*\mathbf{C}\mathbf{w}_2$ of any scan point $\vec{\xi}$ with the peak location $\vec{\xi}_{\mathrm{max}}$ is determined entirely by $\mathbf{C}_{\mathrm{max}}$. In other words:

$$\mathbf{w}^*\mathbf{C}\mathbf{w}_{\mathrm{max}} = \mathbf{w}^*\mathbf{C}_{\mathrm{max}}\mathbf{w}_{\mathrm{max}} \tag{35}$$

for all possible $\mathbf{w}$. This is satisfied when

$$\mathbf{C}\mathbf{w}_{\mathrm{max}} = \mathbf{C}_{\mathrm{max}}\mathbf{w}_{\mathrm{max}} . \tag{36}$$

Equation (36) does not have a unique solution for $\mathbf{C}_{\mathrm{max}}$, but it does when we write

$$\mathbf{C}_{\mathrm{max}} = A_{\mathrm{max}}\mathbf{h}\mathbf{h}^* . \tag{37}$$

The solution of (36) with (37) is

$$\mathbf{h} = \frac{\mathbf{C}\mathbf{w}_{\mathrm{max}}}{A_{\mathrm{max}}} , \tag{38}$$

and, consequently,

$$\mathbf{C}_{\mathrm{max}} = \frac{\mathbf{C}\mathbf{w}_{\mathrm{max}}\mathbf{w}_{\mathrm{max}}^*\mathbf{C}}{A_{\mathrm{max}}} . \tag{39}$$

Herewith, we have an alternative for (34) that does not make use of the transfer vector $\mathbf{g}_{\mathrm{max}}$, except to define the weight vector $\mathbf{w}_{\mathrm{max}}$. It is noted that $\mathbf{h} = \mathbf{g}_{\mathrm{max}}$ if (34) holds.

35

For wind tunnel measurements, source removal using CLEAN gives generally better results than principal component removal. Using CLEAN, the approximation (39) gives better results than (34). It gives no complications, when the beamforming is started without the main diagonal of **C**. As soon as an updated cross-power matrix is introduced by step 2 (see above), then the main diagonal can no longer be neglected.